J. Appl. Comput. Mech., xx(x) (2026) 1-15
DOI: 10.22055/jacm.2026.49257.5844

ISSN: 2383-4536
jacm.scu.ac.ir

Shahid Chamran University of Ahvaz

Journal of Applied and Computational Mechanics

Research Paper

A 2D Adaptive Finite Element-Discrete Element Coupling Algorithm for Impact Dynamics

Zhibin Li, Xu Cheng, Banghai Jiang

College of Science, National University of Defense Technology, Changsha, Hunan 410073, PR China

Received April 12 2026; Revised May 26 2026; Accepted for publication May 28 2026.
Corresponding author: Z. Li (lizhibin@nudt.edu.cn)
© 2026 Published by Shahid Chamran University of Ahvaz

Abstract. Meshfree methods offer excellent adaptivity, versatility, and robustness, and show great potential for solving problems intractable to conventional numerical methods. In the present study, an adaptive two-dimensional finite element (FE)-discrete element (DE) coupling algorithm is developed by incorporating the discrete element method (DEM) into continuum analysis and synergistically combining the finite element method (FEM) with DEM. By employing the Mohr-Coulomb fracture criterion, the adaptive transition from continuum to discontinuum is realized within the proposed FE-DE framework. The accuracy and effectiveness of the present method are validated through numerical simulations of the dynamic response of a two-dimensional plate under impulsive loading. Furthermore, the applicability and performance of the adaptive FE-DE algorithm are further examined via simulations of dynamic fracture in notched semi-circular rock specimens and penetration of concrete targets by rigid projectiles. Numerical results demonstrate that the proposed method is feasible and competent for simulating impact-induced failure and dynamic fracture processes.

Keywords: FE-DE Coupling, FEM, DEM, Adaptive Transition, Dynamic Failure.

1. Introduction

Traditional numerical methods represented by the finite element method (FEM) [1] are established on continuum mechanics, which inherently limits their capability to simulate the entire continuous-to-discontinuous failure evolution of solid materials. For dynamic failure and progressive fracture of engineering materials and structures under high-strain-rate impact loads [2, 3], conventional mesh-based continuum methods generally adopt mesh erosion and deletion techniques to characterize material fracture. However, such treatments inevitably introduce inherent numerical defects, including frequent mesh remeshing operations [4], artificial mass loss, and unphysical stress fluctuation. Although refined element processing and modified fracture criteria have been adopted to improve simulation performance, accurate and stable modeling of full-range dynamic fracture, from elastic deformation to large deformation and final fragmentation, remains a challenging problem for traditional pure FEM.

Different from continuum-based FEM, the discrete element method (DEM) [5] discretizes materials into independent discrete particles and explicitly solves particle contact, collision, and friction behaviors, exhibiting unique advantages in simulating discontinuous deformation and fracture evolution. This feature enables DEM to be widely applied in granular flows, fracture mechanics, and multiphase mechanical analysis [6, 7], especially for brittle materials such as rock and ceramic under quasi-static and dynamic loading [8, 9]. In practical engineering, DEM has been extensively used for mechanical analysis of concrete and geomaterials in civil engineering [10, 11], as well as for robot–granular medium interaction simulation in aerospace engineering [12]. Nevertheless, DEM suffers from prominent computational bottlenecks: massive particle contact searching and iterative interaction calculation lead to extremely high computational complexity, which severely restricts its application in large-scale engineering impact dynamic problems [13, 14]. Accordingly, coupling FEM and DEM has become a mainstream technical route to simultaneously guarantee computational accuracy and efficiency for dynamic damage and fracture simulations.

Hybrid FEM-DEM coupling methods [15] integrate the respective superiorities of continuum and discontinuum algorithms, which are highly suitable for solving complex engineering problems with coexisting continuous deformation and localized discontinuous failure. In typical coupling frameworks, FEM undertakes high-efficiency calculation of low-damage intact domains, while DEM is activated adaptively in localized damage, large deformation and fracture regions. This complementary coupling mechanism provides a robust numerical platform for impact dynamic fracture analysis, enabling comprehensive capture of fracture initiation, propagation and final fragmentation under complex dynamic loading [16]. Existing coupling techniques have been successfully applied to rock blasting, tunnel excavation, and hydraulic fracturing simulations [17]. Færgestad et al. [18] implemented a coupled FEM-DEM in LS-DYNA to simulate hypervelocity impacts of aluminium projectiles on aluminium targets. Deng and Liu [19] adopted the combined finite–discrete element method (FDEM) to explore the mechanical properties and failure

Published online: August 14 2026

mechanisms of soil–rock mixtures. Hubert et al. [20] performed transient FEM-DEM coupling analysis to investigate brake squeal behaviors. Cao et al. [21] proposed a local conversion FEM-DEM method for rock crack modeling.

Despite the widespread application of continuum–discontinuity coupling algorithms, current mainstream methods still possess inherent limitations in high-strain-rate impact dynamics and progressive fracture simulation, corresponding to insufficient computational efficiency, poor adaptive capacity and incomplete physical conservation. Traditional fixed FEM–DEM coupling methods rely on empirical predefinition of discrete coupling regions, which only performs well for predictable fracture morphology but fails to adaptively capture stochastic crack initiation and random fragmentation under complex impact loading. Adaptive remeshing-based coupling FEM improves local simulation resolution through dynamic mesh reconstruction, whereas iterative remeshing introduces additional computational overhead and potential numerical instability, and cannot realize the physical transition from continuous medium to discrete fragments. As a classic continuum-discontinuity method, FDEM embeds fracture criteria into continuum elements to simulate crack propagation; however, its simplified domain conversion and interface processing cannot strictly satisfy mass, momentum and energy conservation, easily causing local stress deviation and cumulative energy drift under ultra-high strain-rate dynamic loading. Commercial coupling modules in LS-DYNA adopt empirical conversion rules to balance efficiency, while physical conservation constraints are not fully guaranteed during domain transformation, compromising numerical stability and result reproducibility in impact and penetration simulations. In addition, most existing studies focus on static or quasi-static fracture problems, while systematic optimization and quantitative validation for dynamic impact scenarios are insufficient. Furthermore, conventional coupling methods lack targeted adaptive strategies driven by real-time material damage, resulting in unreasonable matching between continuous/discrete domains and poor accuracy-efficiency balance.

To address the above research gaps, this study develops a novel two-dimensional adaptive FEM–DEM coupling algorithm tailored for impact dynamic fracture simulation. Different from fixed coupling and remeshing-based methods, the proposed method establishes a damage-driven real-time domain adaptive transition mechanism, eliminating artificial region partitioning and mesh remeshing dependence. Strict mass, momentum and energy conservation mapping is supplemented during FEM-to-DEM conversion to eliminate unphysical numerical errors. Unified interface discretization, bidirectional synchronous data transmission and matched time-step stability criteria are developed to improve numerical robustness. Finally, three typical dynamic benchmark cases, including plate stress wave propagation, rock dynamic fracture and concrete penetration, are adopted to verify the superiority of the proposed method in balancing global continuous response accuracy and local fracture resolution, and comprehensive quantitative comparisons with pure FEM, pure DEM, remeshing-based FEM, XFEM, SPH and conventional FDEM are conducted to demonstrate its computational performance and engineering applicability.

2. Continuum Discrete Element Model

2.1. 2D Continuum discrete element model

The fundamental principle of DEM is to discretize the computational domain into discrete elements and characterize material mechanical responses through inter-element interaction models. Traditional DEM is originally designed for discontinuous granular problems and only activates compressive contact behavior without tensile bearing capacity. To extend DEM to continuum mechanical analysis, connective models with both tensile and compressive resistance are adopted to bond discrete elements together. When material damage accumulates to satisfy the fracture criterion, the connective bonds fail and convert into contact pairs, realizing the transition from continuous medium to discontinuous fragments.

In this study, aiming at plane stress problems, the elastic computational domain is discretized into rigid disc elements, as illustrated in Fig. 1 [22, 23]. Three typical disc arrangement modes are available, among which the seven-disc model (Type A) and nine-disc model (Type B) possess regular topological structures and are suitable for continuum simulation, while the arbitrary arrangement model (Type C) cannot guarantee mechanical continuity and is thus excluded. Discrete discs are connected by normal and tangential springs following Hooke's law, with stiffness coefficients k_n and k_s, respectively. The spring parameters are directly derived from continuum elastic constitutive relations, enabling the discrete disc system to reproduce the elastic mechanical behavior of continuous materials. For complex nonlinear constitutive responses, corresponding connection element modules can be further extended.

Interactions only occur between adjacent discrete elements without long-range force transmission. Neighbor searching is essential for contact force calculation but brings considerable computational consumption. Therefore, an efficient pre-search algorithm is adopted in this study to reduce redundant traversal calculation and improve overall computational efficiency [24].

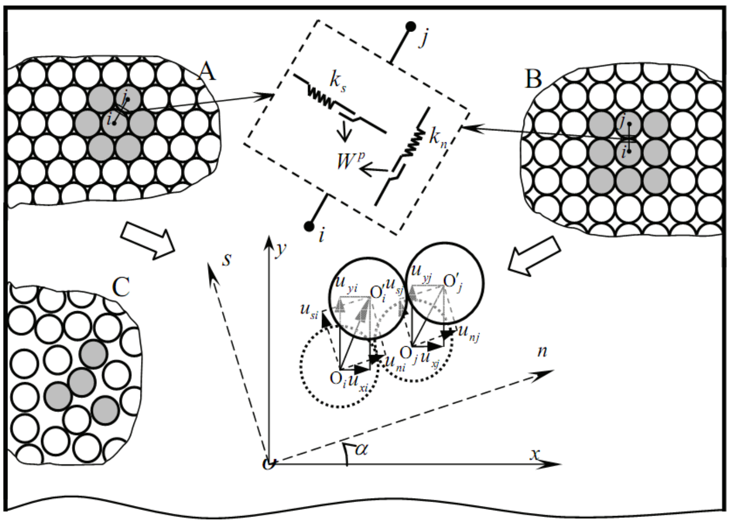

Fig. 1. DEM models based on rigid disc elements [22, 23].

2.2. Interaction forces

The inter-element interaction force model constitutes the core of DEM numerical calculation, which dominates momentum and energy conservation and determines the dynamic mechanical responses of materials under impact loading. In this study, the elastic spring stiffness coefficients are derived via the elastic potential energy equivalence method, ensuring the consistency between discrete element responses and continuum mechanical theory. Taking the central disc i with p adjacent discs in Fig. 1 as the research object, the total elastic potential energy of connected to disc pairs is expressed as:

$$U = \frac{1}{2}\sum_{j=1}^{p}\left[k_{nij}(u_{nj}-u_{ni})^2 + k_{sij}(u_{sj}-u_{si})^2\right] = VU_e \tag{1}$$

where V is the volume of disc element; k_{nij} and k_{sij} represent normal and tangential spring stiffness between discs i and j; u_{ni}, u_{si}, u_{nj} and u_{sj} denote normal and tangential displacements of the two discs, respectively.

For homogeneous isotropic elastic materials, the strain-energy density (i.e., deformation energy per unit volume) is defined as:

$$U_e = \frac{1}{2E}\left[\sigma_x^2 + \sigma_y^2 - 2\upsilon\sigma_x\sigma_y + 2(1+\upsilon)\tau_{xy}^2\right] \tag{2}$$

where E and υ are Young’s modulus and Poisson’s ratio of the material, respectively.

The elastic potential energy U in Eq. (1) is equivalent to the strain-energy density in Eq. (2). Thus, by equating the discrete potential energy U and continuum strain energy VU_e, the normal and tangential spring stiffness can be quantitatively derived. Taking the nine-disc regular model (type B in Fig. 1) as shown in Fig. 2, all discs have identical radius r. For orthotropic materials, the calibrated spring coefficients are expressed as:

$$k_{n1} = \frac{E\delta}{2r(1-\upsilon^2)},\quad k_{n2} = \frac{E\delta}{2r\sqrt{2}(1-\upsilon^2)},\quad k_s = \frac{E\delta}{4r(1+\upsilon)} \tag{3}$$

where δ is the disc thickness, k_{n1} denotes the normal spring stiffness between the central disc and orthogonal adjacent discs, k_{n2} corresponds to the diagonal adjacent disc pairs.

The above parameters are applicable to plane stress conditions. For plane strain problems, equivalent Young's modulus E^* and equivalent Poisson's ratio υ^* are adopted:

$$E^* = \frac{E}{1-\upsilon^2},\quad \upsilon^* = \frac{\upsilon}{1-\upsilon} \tag{4}$$

Considering the plastic deformation characteristics of materials under impact loading, a bilinear elastoplastic constitutive model is introduced for discrete elements, with elastic unloading assumed in the deformation rebound stage. The piecewise mechanical relation of spring force and displacement increment is written as:

$$f_\alpha = \begin{cases} k_\alpha \cdot \Delta u_\alpha, & (|f_\alpha| \le f_\alpha^y) \\ f_\alpha^y + k'_\alpha \cdot (\Delta u_\alpha - \Delta u'_\alpha), & (|f_\alpha| > f_\alpha^y) \end{cases} \tag{5}$$

where f_α is the spring interaction force, Δu_α is the displacement increment, f_α^y is the plastic yield force, k_α and k'_α represent elastic and plastic spring coefficients, respectively. The subscript α denotes normal (n) and tangential (s) directions. Within a single time-step, linear elastic behavior is adopted when the interaction force is lower than the yield threshold, while plastic hardening behavior is activated once yielding occurs, with the yield criterion updated in real time.

It is noteworthy that the adopted simplified bilinear elastoplastic model can effectively capture the basic elastic–plastic deformation, crack initiation and propagation of metallic and quasi-brittle materials under medium-and-high strain-rate impact loading. However, this model simplifies the complex post-peak softening characteristics of quasi-brittle materials and cannot fully reproduce fine-scale microcrack evolution.

In addition, the current constitutive framework is limited to two-dimensional planar simulation, lacking three-dimensional spatial mechanical characterization capability. These inherent limitations are explicitly acknowledged, and corresponding optimization will be implemented in future work.

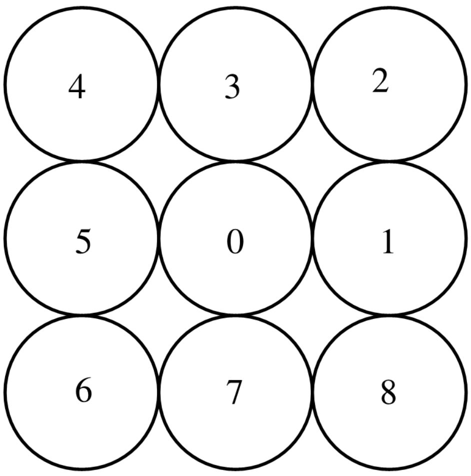

Fig. 2. Nine-disc model of DEM.

2.3. Fracture criterion

The Mohr-Coulomb failure criterion [25] with tensile cut-off is adopted to judge bond failure and realize the continuum to discontinuum transition. The tensile failure condition of inter-element connective bonds is defined as:

$$\frac{|f_n|}{S} \geq \sigma_t S \lambda \tag{6}$$

where f_n is the normal tensile force on the contact interface, σ_t is the material tensile strength, and S is the effective contact area.

Initially, adjacent discrete elements are connected by elastic springs to bear compression, tension, and shear, maintaining material continuity. Once the tensile force exceeds the failure threshold, the connective bond fails and is converted into a pure contact pair, which only bears compressive and frictional forces. A contact damping coefficient λ (0.4-0.6) is introduced to calculate post-failure interaction forces, and the contact spring stiffness is revised as:

$$k_n^* = \lambda k_{n1}, \quad k_s^* = \lambda k_s \tag{7}$$

The revised contact model consists of stiffness springs, damping dashpots, and friction sliders, which can accurately characterize the collision, extrusion and sliding behaviors of fragmented materials after fracture.

2.4. Basic equations

For adjacent element pairs i and j, the relative normal and tangential displacement increments within a single time step Δt are derived from nodal displacement variations:

$$\begin{cases} \Delta u_n = (\Delta u_{xj} - \Delta u_{xi})\cos\theta + (\Delta u_{yj} - \Delta u_{yi})\sin\theta \\ \Delta u_s = (\Delta u_{xj} - \Delta u_{xi})\sin\theta + (\Delta u_{yj} - \Delta u_{yi})\cos\theta \end{cases} \tag{8}$$

where θ is the included angle between the element centerline and the horizontal coordinate axis; $\Delta u_{xi}, \Delta u_{xj}, \Delta u_{yi}, \Delta u_{yj}$ are displacement increments of the two elements in *x* and y directions.

According to Hooke's law, the normal and tangential interaction forces on the contact interface are determined by spring stiffness and relative displacement:

$$\begin{cases} f_n = k_n \cdot \Delta u_n \\ f_s = k_s \cdot \Delta u_s \end{cases} \tag{9}$$

The resultant force and moment acting on each discrete element are accumulated from all adjacent contact interactions. The dynamic equilibrium equation of element *i* is established based on Newton's second law:

$$\begin{cases} F_{xi} = \sum\left(f_n \cos\theta - f_s \sin\theta\right) \\ F_{yi} = \sum\left(f_n \sin\theta + f_s \cos\theta\right) \\ M_i = \sum r\left(f_n \sin\theta + f_s \cos\theta\right) \end{cases} \tag{10}$$

$$\begin{cases} m_i \cdot \ddot{x}_i(t) = F_{xi} \\ m_i \cdot \ddot{y}_i(t) = F_{yi} \\ I_i \cdot \ddot{\phi}_i(t) = M_i \end{cases} \tag{11}$$

where m_i is element mass; $\ddot{x}_i(t)$, $\ddot{y}_i(t)$ and $\ddot{\phi}_i(t)$ are linear accelerations and angular acceleration, respectively. The central difference method, consistent with explicit FEM, is adopted for time integration to update velocity, displacement, and rotation variables, laying a foundation for subsequent adaptive FE-DEM coupling algorithm development.

3. Adaptive Finite Element-Discrete Element Method

3.1. Combination model of the FE and DE domains

The core of high-precision FE–DEM coupling lies in realizing seamless physical field transition and consistent dynamic response between continuous and discrete domains. Both FEM and DEM adopt explicit central difference time integration and follow Newton's motion equation, possessing inherent algorithm compatibility. In this study, FE-DEM composite elements are defined at the coupling interface to realize bidirectional force and motion transmission. Composite elements share nodal information with FEM domain elements and participate in contact force calculation as DEM particles, acting as the bridge connecting continuous and discrete domains.

To guarantee geometric matching and mechanical compatibility, the nine-disc DEM model with regular topology is matched with four-node rectangular FEM elements, as shown in Fig. 3. All coupling calculations adopt unified time increment, which simultaneously satisfies the stability criteria of FEM continuum wave propagation and DEM particle contact oscillation. The elastoplastic constitutive framework is consistent in both domains, ensuring no physical mutation during domain transformation. The dynamic equilibrium equation of composite elements considering FEM nodal force, DEM contact force and external load is established as:

$$m\ddot{u} = F_{int} + F_{nodal} + F_{ext} F_{nodal} m_i \tag{12}$$

where F_{int} is the inter-element interaction force, F_{nodal} is the nodal force, and F_{ext} is the external force.

3.2. Adaptive conversion model of FEs to DEs

Different from traditional fixed coupling methods, the proposed algorithm realizes damage-driven fully automatic FE-to-DEM domain transition without artificial preset partition. The explicit dynamic FEM adopts lumped mass distribution, which matches the particle mass characteristic of DEM and ensures physical consistency of state variable transmission. An equivalent plastic strain-based adaptive conversion criterion is established: when the accumulated plastic strain of a finite element exceeds the critical threshold under impact loading, the severely damaged element is automatically converted into four discrete particles as illustrated in Fig. 4, with particle centroids coinciding with original FEM nodes. During conversion, element mass is evenly inherited by new discrete particles to eliminate mass loss; kinematic variables including velocity, displacement, and acceleration are spatially averaged and directly assigned, ensuring continuous dynamic responses before and after conversion. After element invalidation and mesh deletion, the overall computational domain remains continuously connected, avoiding solution discontinuity.

The equivalent plastic strain $\bar{\varepsilon}^p$ is selected as the conversion indicator to characterize material damage degree, which is defined as:

$$\bar{\varepsilon}^p = \sqrt{\frac{2}{3}\varepsilon_{ij}^p \varepsilon_{ij}^p} \tag{13}$$

where ε_{ij}^p denotes plastic strain tensor components. The adaptive conversion criterion is expressed as:

$$\bar{\varepsilon}^p \geq \bar{\varepsilon}_{\text{crit}}^p \tag{14}$$

where $\bar{\varepsilon}_{\text{crit}}^p$ is the critical equivalent plastic strain threshold. Material-specific critical thresholds are calibrated: $\bar{\varepsilon}_{\text{crit}}^p = 0.02$ for quasi-brittle rock and concrete, and $\bar{\varepsilon}_{\text{crit}}^p = 0.5$ for metallic materials including steel and aluminum. The threshold value is carefully optimized through parametric analysis: a lower threshold causes premature conversion and redundant computational consumption, while an excessively high threshold suppresses effective fracture characterization and leads to mesh distortion. The adopted threshold balances numerical stability, simulation accuracy and computational efficiency for medium-and-high strain-rate progressive fracture problems.

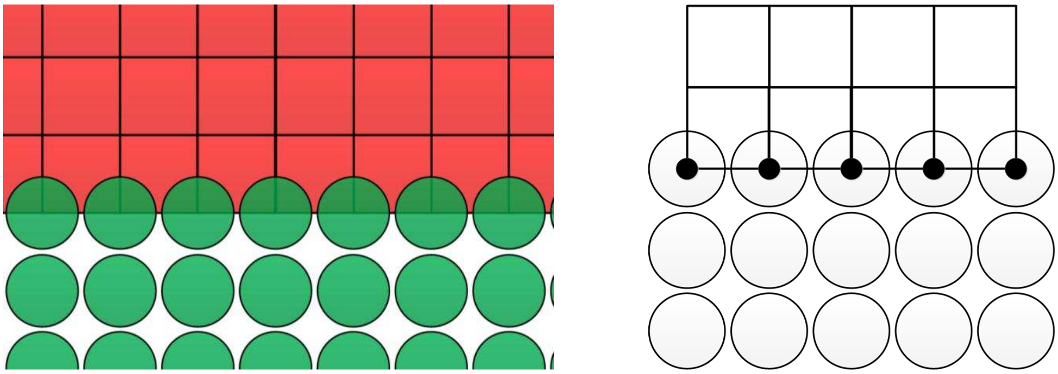

(a) (b)

Fig. 3. Combination of the DEM and FEM domains, (a) Combination of the nine-disc model of DEM and the four-node rectangular element of FEM, (b) Schematic of the transition layer on the boundary.

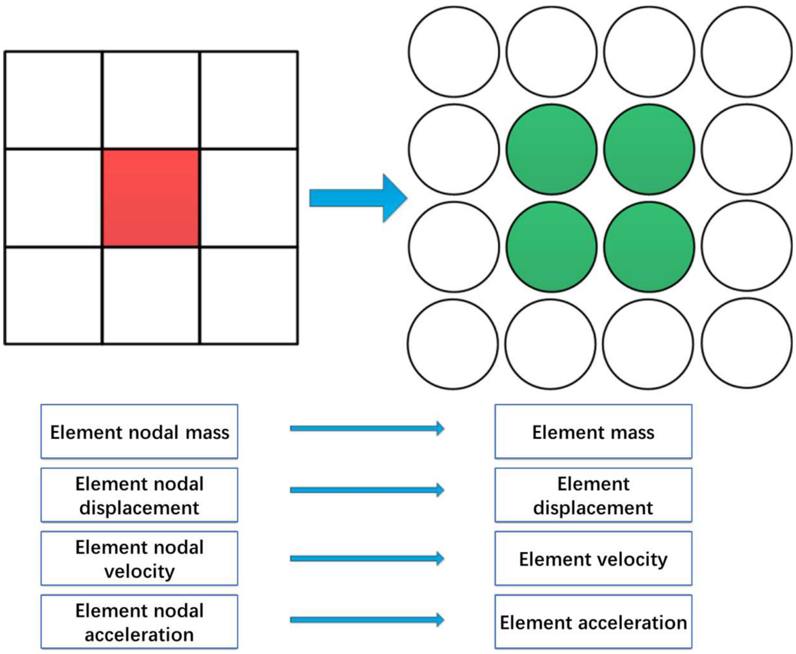

(a)

Fig. 4. Adaptive conversion process of FE domain.

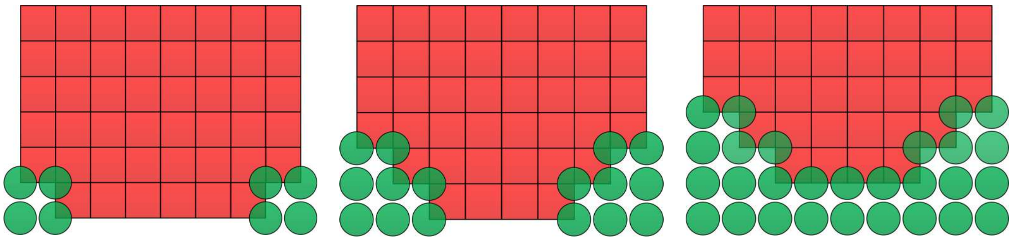

Fig. 4. Continued.

3.2.1. Fundamental conservation principle during FEM-DEM adaptive conversion

To eliminate unphysical numerical errors widely existing in conventional coupling methods and commercial solvers, strict mass, momentum, and kinetic energy conservation constraints are implemented throughout the adaptive conversion process. For a single FEM element with mass m_e converted into N_p discrete particles, each particle is assigned equal mass $m_p = m_e / N_p$, ensuring total mass conservation without artificial mass gain or loss.

For momentum conservation, the element average velocity $\bar{v}_e$ obtained by Gaussian integration is uniformly assigned to new particles, ensuring continuous system momentum before and after conversion:

$$m_e\bar{v}_e = \sum m_p\bar{v}_p \tag{15}$$

To solve minor kinetic energy deviation caused by continuum–discontinuum state transition, a velocity scaling correction coefficient λ is introduced to strictly guarantee kinetic energy consistency $(E_{k,p} = E_{k,e})$ without changing total momentum:

$$E_{k,e} = \frac{1}{2}m_e\bar{v}_e^2, \quad E_{k,p} = \sum \frac{1}{2}m_p\bar{v}_p^2 \tag{16}$$

At the coupling interface, penalty-based contact constraints and velocity compatibility conditions are adopted to suppress unphysical energy dissipation and interfacial penetration. A unified time-step stability criterion avoids cumulative energy drift in long-term dynamic fracture evolution, significantly improving numerical robustness compared with conventional FDEM and commercial coupling algorithms.

3.2.2. Numerical treatment of FEM-DEM coupling interface

A unified interface discretization and bidirectional synchronous data transmission framework is developed to guarantee interfacial numerical stability. FEM boundary domains are discretized by quadratic isoparametric elements with Gaussian integration points for force calculation. Bounding box detection is performed in each time step to screen coupling candidate particles, and the discretization resolution is matched to ensure that the boundary segment length is 1.0–1.5 times the particle diameter, eliminating interfacial gaps and penetration.

For kinematic variable transmission, DEM particle displacement and velocity are interpolated from FEM nodal field via element shape functions to maintain interfacial kinematic compatibility:

$$u_p = \sum_{i=1}^{n_{node}} N_i(\xi,\eta)u_i, \quad v_p = \sum_{i=1}^{n_{node}} N_i(\xi,\eta)v_i \tag{17}$$

where u_p, v_p stand for particle displacement and velocity; $N_i(\xi,\eta)$ is element shape function; u_i, v_i refer to displacements and velocities of FEM boundary nodes. The interpolation scheme suppresses abnormal velocity mutation and interfacial separation, guaranteeing kinematic consistency of the coupled domain.

For mechanical variable mapping, discrete particle contact forces are homogenized and converted into continuous boundary traction based on virtual work equivalence, and equivalent FEM nodal forces are obtained by Gaussian integration to avoid local stress concentration and numerical oscillation:

$$\delta W = F_p \cdot \delta u_p = T_e \cdot \delta u_e \tag{18}$$

in which δW denotes virtual work, F_p is particle contact force, and T_e represents equivalent boundary traction. This mapping approach prevents local stress concentration and numerical oscillation induced by discrete loads.

An adaptive penalty stiffness method is adopted for interface contact, with stiffness calibrated according to material elastic modulus and mesh size to achieve non-penetration constraints without excessive numerical stiffness. A field smoothing algorithm is further applied to filter high-frequency numerical noise generated by adaptive domain conversion, ensuring stable long-term dynamic simulation.

3.2.3. Time step stability and element/disc size influence

A dual constrained unified stable time-step criterion is proposed for the coupled system, considering elastic wave propagation in FEM domains and particle contact oscillation in DEM domains. The critical time step of FEM is determined by minimum element size and elastic wave velocity:

$$\Delta t_{FEM} \le \alpha\frac{h_{min}}{c_d}, \quad c_d = \sqrt{\frac{E}{\rho(1-\nu^2)}} \tag{19}$$

where h_{min} is the minimum FEM element size, c_d is the plane-stress elastic wave velocity, E, ρ and ν denote Young's modulus, density and Poisson's ratio, respectively, and $\alpha = 0.85$ is a stability reduction coefficient to accommodate dynamic fracture and adaptive domain conversion.

The critical time step of DEM is constrained by particle mass and contact stiffness to suppress unphysical penetration:

$$\Delta t_{DEM} \le \beta\sqrt{\frac{m_{min}}{k_n}} \tag{20}$$

where m_{min} is the minimum particle mass, k_n is the normal contact stiffness, and $\beta = 0.15$ is a safety coefficient for discrete contact calculation. The final adaptive time step is taken as the minimum value of the two critical steps, i.e. $\Delta t = min(\Delta t_{FEM}, \Delta t_{DEM})$, eliminating temporal scale mismatch between continuous and discrete domains.

Element and particle sizes significantly affect simulation accuracy, fracture morphology and computational cost. Parametric sensitivity analysis indicates that the optimal FEM element size is 1/20–1/40 of the structural characteristic length for impact fracture simulation. Reasonable matching between element size and particle diameter ensures interfacial force transmission stability and avoids abnormal conversion. The calibrated size matching principle effectively improves the numerical reproducibility and reliability of the proposed coupling algorithm.

Benefiting from the above adaptive conversion and interface processing strategies, the proposed method avoids repeated mesh reconstruction required by remeshing-based FEM, realizes automatic domain transition driven by real-time material damage, and effectively balances numerical accuracy and computational efficiency for impact dynamic fracture problems.

4. Numerical Results and Discussions

A self-developed explicit dynamic calculation program is compiled based on the proposed 2D adaptive FEM-DEM coupling algorithm. Typical benchmark cases including plate stress wave propagation, rock dynamic fracture and concrete penetration are simulated for verification. Comprehensive quantitative comparisons with pure FEM, pure DEM, remeshing-based FEM, XFEM, SPH and conventional FDEM are conducted in terms of simulation accuracy, CPU runtime, memory consumption and parallelization potential to fully demonstrate the algorithm performance.

4.1. Verification of the adaptive FE-DE coupling algorithm

A 2D steel plate impact model is established to verify the interfacial transmission accuracy and algorithm stability of the coupling method. The steel plate has a dimension of 30 mm × 60 mm × 10 mm, density of 7.8 g/cm^3, elastic modulus of 232 GPa and Poisson's ratio of 0.3. An impulse pressure load of $p = 500$ MPa with a duration $t_d = 3$ μs is applied on the left boundary. Two partition cases (upper–lower partition and left–right partition) are designed to verify the wave transmission performance across FE–DE coupling interfaces, as illustrated in Fig. 5.

4.1.1. *Modeling and results of case A*

As shown in Fig. 5(a), in the upper-lower partition model of Case A, the upper FE domain was meshed into 1024 elements with a side length of 0.9375 mm, while the lower DE domain was meshed into 1105 elements with a radius of 0.46875 mm. When the impulsive load was applied to the left side of the plate, stress waves propagated into the plate through both the upper and lower parts at the same velocity. Points a and b were selected from the upper and lower parts of the plate, respectively, to record the velocity and stress time-history curves at different positions during the impact process. Point *a* was located in the FE domain and calculated using FEM, while Point *b* was located in the DE domain and calculated using DEM. The stress wave propagation law was analyzed, and the dynamic response differences between the upper and lower regions of the plate were compared.

The velocities and stresses of Points a and b are shown in Fig. 6. From Fig. 6(a), it can be observed that the velocity curves of the two points are in general agreement, indicating that the DEM and FEM satisfy the displacement continuity condition in continuum calculation and can be matched, providing a basis for the subsequent construction of the coupling model. Combined with the stress curve comparison results in Fig. 6(b), the plateau of the stress curves of the two points agrees reasonably well, demonstrating uniform stress transmission in the FE-DE coupling region and reliable algorithm matching, which further verifies the reliability of this coupling mechanism. However, there is a certain deviation in the particle velocity obtained by the two algorithms during the unloading stage, which may be attributed to differences in the node force calculation models of FEM and DEM. In FEM, node forces are calculated based on the principle of virtual work, while in DEM, forces are solved through a particle contact mechanics model, resulting in slight differences in velocity variation. Similarly, a deviation exists in the stress of the two points during the unloading stage; a possible reason is the difference in stress calculation algorithms between the two methods. In FEM, stress is solved using the elastic matrix and strain, while in DEM, stress is converted from particle contact force and contact area.

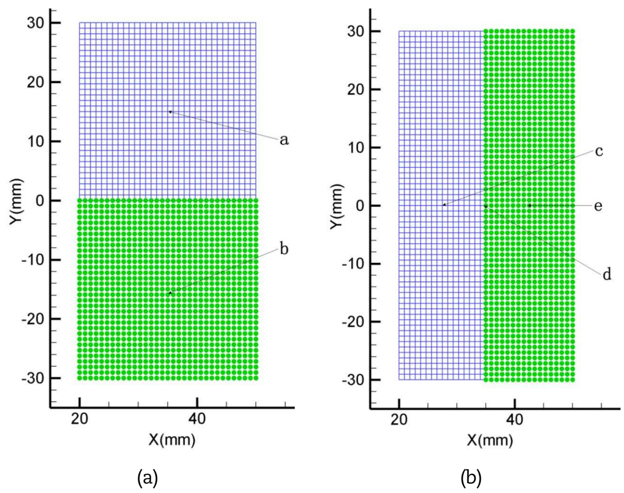

Fig. 5. Computational domain of the plate in different cases, (a) Case A, (b) Case B.

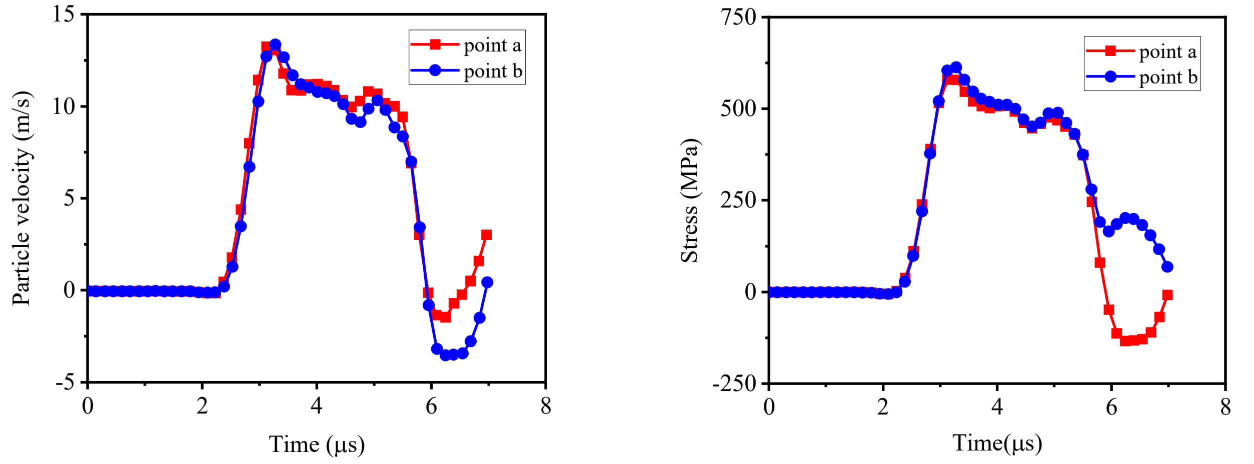

(a) (b)

Fig. 6. Comparison of the results in FE and DE domains for case A, (a) Comparison of the particle velocity, (b) Comparison of the stress.

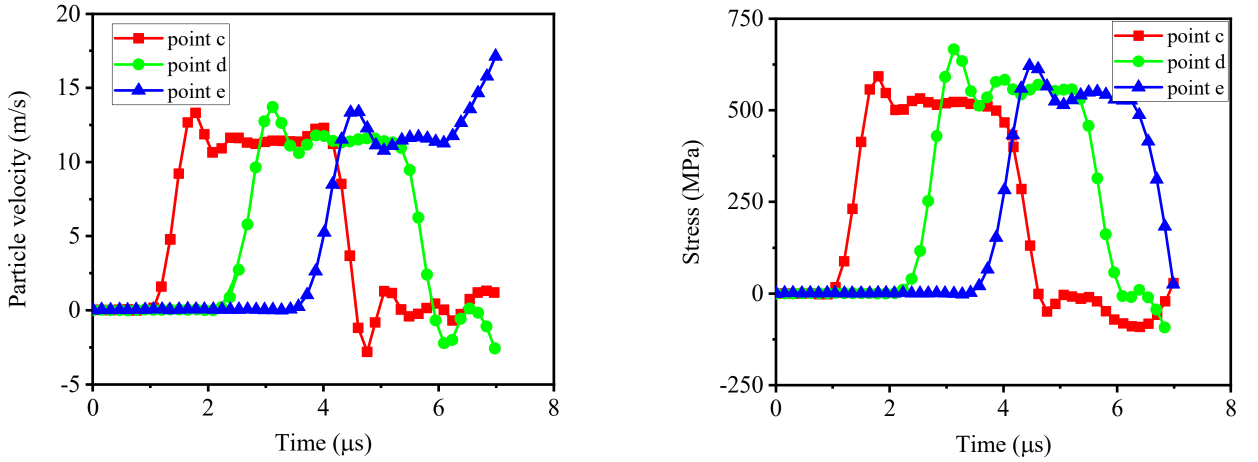

(a) (b)

Fig. 7. Comparison of the results in FE and DE domains for case B, (a) Comparison of the velocity, (b) Comparison of the stress.

4.1.2. *Modeling and results of case B*

As shown in Fig. 5(b), in the left-right partition model of Case B, the left FE domain was meshed into 1024 elements with a side length of 0.9375 mm, while the right DE domain was meshed into 1089 elements with a radius of 0.46875 mm. When the impulsive load was applied to the left side of the plate, the stress wave first propagated through the left FE domain, and then through the right DE domain. By examining the impact responses of materials at different sampling points in the left and right domains, the influence of the FE-DE transition boundary on stress wave propagation was investigated. A sudden change in the stress time-history curves of sampling points on both sides of the boundary would indicate interference of the boundary with wave propagation.

Points *c*, *d*, and *e* were selected in the left and right parts of the computational domain, with their specific locations shown in Fig. 5(b). Point *c* was located in the FE domain and calculated using FEM. Point *d* was situated on the FE-DE transition boundary (as a FE-DE composite element), and its calculation required FE-DE algorithm coupling. Point *e* was located in the DE domain and computed using DEM. The velocities and stresses of points *c*, *d*, and *e* are shown in Fig. 7.

As can be seen from Fig. 7, the peak particle velocities of the three points are identical, and their velocity waveforms are in good agreement, indicating that the shock wave can propagate smoothly through the transition boundary of the homogeneous material and travel within both the FE and DE domains. The consistency of the stress peaks at Points *c*, *d*, and *e* demonstrates the computational effectiveness of the FEM-DEM transition boundary. Additionally, the simulation results are in good agreement with the theoretical values, verifying the feasibility of the proposed method.

4.1.3. *Analysis of results for case A and case B*

Based on stress wave theory, the shock wave velocities, maximum stresses, and particle velocities at different points in the plate can be derived. The theoretical values of these parameters were compared with the numerical simulation results, as shown in Tables 1 and 2.

The velocity and stress time-history responses of typical monitoring points show good consistency between FEM and DEM domains. The particle velocity and shock wave velocity errors of the proposed coupling method are controlled within 4% and 3%, respectively, verifying reliable interfacial continuity and stable wave propagation. Minor local stress deviation exists in the unloading stage, which originates from the inherent difference between FEM field-based stress solution and DEM contact-based stress calculation.

Quantitative comparison results in Table 1 and Table 2 further demonstrate that the proposed adaptive coupling method possesses higher simulation accuracy than pure FEM and pure DEM. Different from pure DEM with severe discrete stress fluctuation and pure FEM with mesh distortion defects, the proposed method maintains smooth stress field transmission in continuous domains and reliable fracture characterization in damaged regions.

Table 1. Comparison of theoretical and numerical results for stress and particle velocity.

	Monitor point	a	b	c	d	e
Particle velocity	Theoretical result (m/s)			11.7537		
	Numerical result (m/s)	11.3793	11.4294	11.4153	11.5396	11.6750
	Relative error (%)	3.19	2.76	2.88	1.82	0.67
Maximum stress	Theoretical result (m/s)			500		
	Numerical result (m/s)	509.92	523.70	518.44	549.84	532.54
	Relative error (%)	1.98	4.74	3.69	9.97	6.51

Table 2. Comparison of theoretical and numerical results for shock wave velocity.

Computation Domain	FEM in case A	DEM in case A	FEM in case B	DEM in case B
Theoretical result (m/s)		5453.8		
Numerical result (m/s)	5387.9	5296.6	5506.7	5494.0
Relative error (%)	1.21	2.88	0.97	0.73

4.2. Comparison of computational efficiency

The computational efficiency of FEM and DEM was investigated and compared using the self-developed computational code. The example model adopted the same 2D plate impact response problem as in Section 4.1, with identical parameters (plate dimensions, material properties, and impact loading conditions).

To compare the relationship between the number of elements and computational load in FEM, the plate was divided into 128, 252, 512, 1152, and 2048 FEs, respectively. For the corresponding DEM models, the plate was divided into 153, 325, 561, 1225, and 2145 DEs. The program was run for 1000 time-steps, and the computation time was recorded as the actual computational load of the algorithm. Each case was calculated three times, and the average computation time was adopted to reduce the impact of varying computer system states. For the same number of elements, FEM and DEM used the same time increment; the correlation between the number of elements and computation speed was studied by comparing the program computation time for different element divisions.

Figure 8 shows the relationship between computation time and the number of elements, comparing FEM, DEM, and DEM using the pre-search algorithm versus the traversal algorithm. It can be seen that as the number of elements increases, the growth rate of the computational load required by DEM is much higher than that of FEM–determined by the different stability requirements of the two methods. The adoption of the pre-search algorithm can effectively reduce the computational load of DEM, and the effectiveness of this algorithm is enhanced as the number of elements increases.

A comparative analysis of computational load under different modeling scenarios was also conducted by comparing the computation time of the Case A and Case B models (Section 4.1) with that of DEM used alone. For the plate divided into 2048 elements, the computation times are presented in Table 3.

As can be seen from Table 3, compared with using DEM alone for the entire computational domain, the coupled FE-DE method can effectively reduce the required computational load. Since the time complexity of the DEM is $O(N^2)$ (where N represents the number of DEs), reducing the number of DEs can significantly shorten the computation time. For Case A and Case B, where half the domain uses FEM and the other half uses DEM, despite reducing the number of DEs by less than 50% and incorporating FEM, the computation time consumed is only 45% to 47% of that of DEM alone. This fully demonstrates the advantages of the coupled FE-DE method.

In addition to pure FEM and pure DEM, further efficiency comparisons are conducted with widely used numerical approaches including remeshing-based FEM, XFEM, SPH and conventional FDEM. Table 4 summarizes the CPU runtime scaling and memory usage under different model scales. Remeshing FEM requires frequent mesh reconstruction for large deformation and fracture, introducing extra overhead and extending runtime. XFEM achieves accurate fracture simulation without mesh refinement but suffers from complicated enrichment function calculation and low computational efficiency for massive cracks. SPH exhibits strong adaptivity to extreme deformation, yet its particle searching and neighbor interaction lead to high time cost. Conventional FDEM adopts fixed coupling regions and full-domain mixed discretization, resulting in heavier computation load than the proposed method.

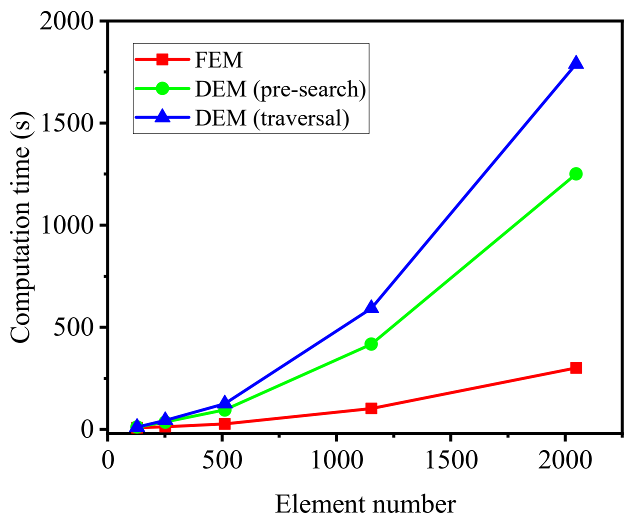

Fig. 8. Relationship between the calculation time and number of elements.

Table 3. Comparison of the computing time for different methods.

Number of elements	Computation time (s)			
	FEM	case A	case B	DEM
2048	300.62	587.97	563.12	1250.94

Table 4. Quantitative comparison of fracture characteristics.

Method	CPU time (s)	Peak memory (MB)	Parallelization performance
Pure FEM (with remeshing)	386.54	216	Good
XFEM	721.39	289	Moderate
SPH	1306.72	425	Fair
Conventional FDEM	612.85	352	Moderate
Proposed method	563.12	241	Excellent

Benefiting from the damage-driven adaptive scheme that limits discrete elements only to failure zones, the present method outperforms the above approaches in overall computational efficiency for impact fracture problems. As the model size increases, the proposed method shows milder growth of CPU time and memory consumption compared with pure DEM and SPH. Furthermore, the algorithm possesses good parallelization potential. The FE domain and independent DEM subdomains can be partitioned and calculated separately, and the variable mapping between domains follows explicit local operations, which is compatible with parallel computing frameworks and can further improve computational efficiency for large-scale engineering models.

4.3. Dynamic fracture of granite

A granite SCB dynamic fracture experiment under SHPB impact loading [26] is adopted to verify the fracture simulation capability of the proposed method. A single-edge notch was pre-fabricated on a semi-circular bend (SCB) rock specimen to measure the dynamic fracture parameters of mode-I fracture. The DEM simulation was verified by comparing experimental and numerical simulation results of crack propagation in the SCB rock specimen under Split Hopkinson Pressure Bar (SHPB) loading (Fig. 9). The SCB specimen had a diameter of 40 mm and a thickness of 1.6 mm. A notch with a width of 1 mm and a length of 5 mm was prefabricated along the axis at the center of the specimen. The material properties of the granite and the steel bar are presented in Table 5. At t = 0, the striker impacted the incident bar of the SHPB at a certain initial velocity to provide the impact loading. The loading force on the SCB specimen is shown in Fig. 9(b).

The element meshing is shown in Fig. 10. FE modeling was adopted for most regions of the SCB specimen to improve computation speed and accuracy, with 628 FEs and an element side length of 1 mm. DE modeling was applied along the potential crack propagation path to facilitate the simulation of material crack propagation. Meanwhile, FE-DE composite elements were defined at the boundary nodes of the computation domain to provide a contact-impact algorithm based on the DE contact model. In the numerical model, the loading force was evenly distributed over the contact surface between the specimen and the incident bar.

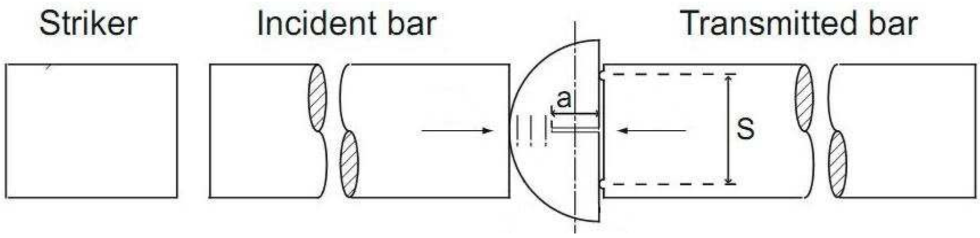

(a)

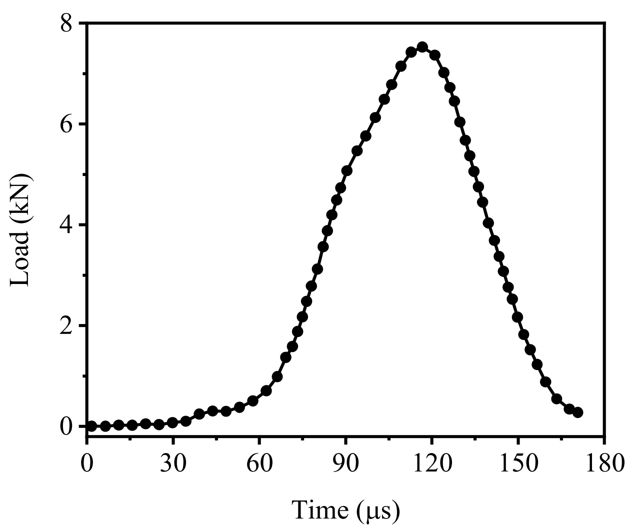

(b)

Fig. 9. Schematics of the experiment setup [26], (a) Schematics of the SPB system and the SCB specimen, (b) Load-time curve on the specimen.

Table 5. Parameters for the material models.

Material	Density (g/cm^3)	Young's modulus (GPa)	Poisson's ratio	Yield strength (MPa)	Plastic modulus (GPa)	Tensile strength (MPa)	Compressive strength (MPa)	Internal force angle
Granite	2.4	92	0.21	8.4	-	2.3	-	-
Concrete	2.4	92	0.21	25.4	-	2.3	-	0.125
Steel	7.8	232	0.3	235	1.879	-	-	-

The element meshing is shown in Fig. 10. FE modeling was adopted for most regions of the SCB specimen to improve computation speed and accuracy, with 628 FEs and an element side length of 1 mm. DE modeling was applied along the potential crack propagation path to facilitate the simulation of material crack propagation. Meanwhile, FE-DE composite elements were defined at the boundary nodes of the computation domain to provide a contact-impact algorithm based on the DE contact model. In the numerical model, the loading force was evenly distributed over the contact surface between the specimen and the incident bar.

By monitoring the status of the interaction model between DEs, the crack propagation behavior in the SCB specimen was obtained. Fig. 11 shows the pressure distribution in the granite SCB specimen at different times. The fracture propagation velocity was estimated using crack gauges in the experiments, with measured average crack propagation velocities of 268 m/s and 355 m/s in two different segments. The corresponding numerical simulation results were 233 m/s and 361 m/s, with relative errors of 13.06% and 1.69%, respectively—confirming the accuracy and applicability of the proposed method.

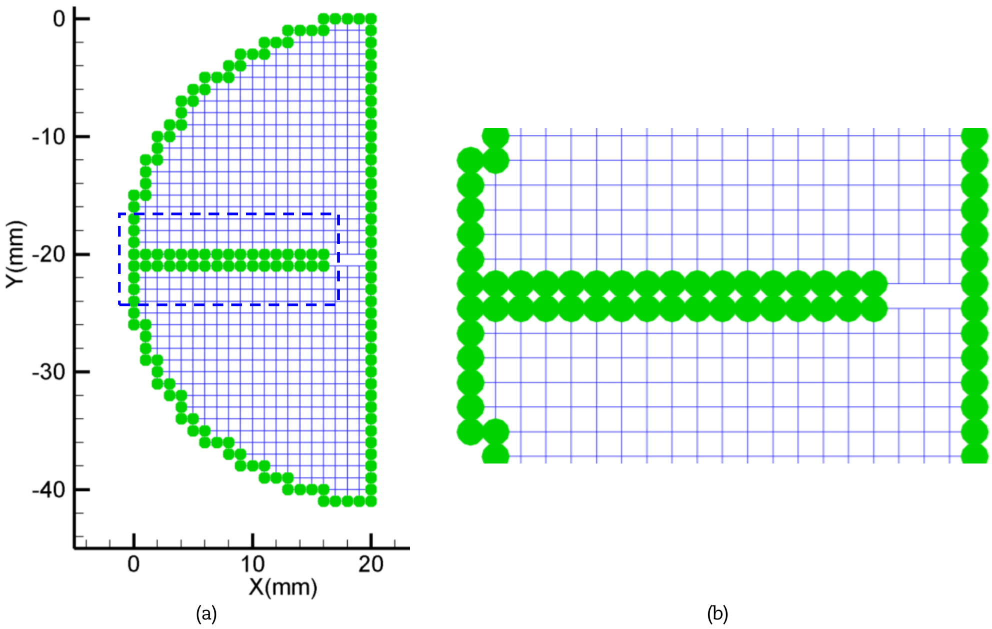

Fig. 10. Numerical model of the granite SCB specimen, (a) Schematic of meshing, (b) Local enlarged drawing.

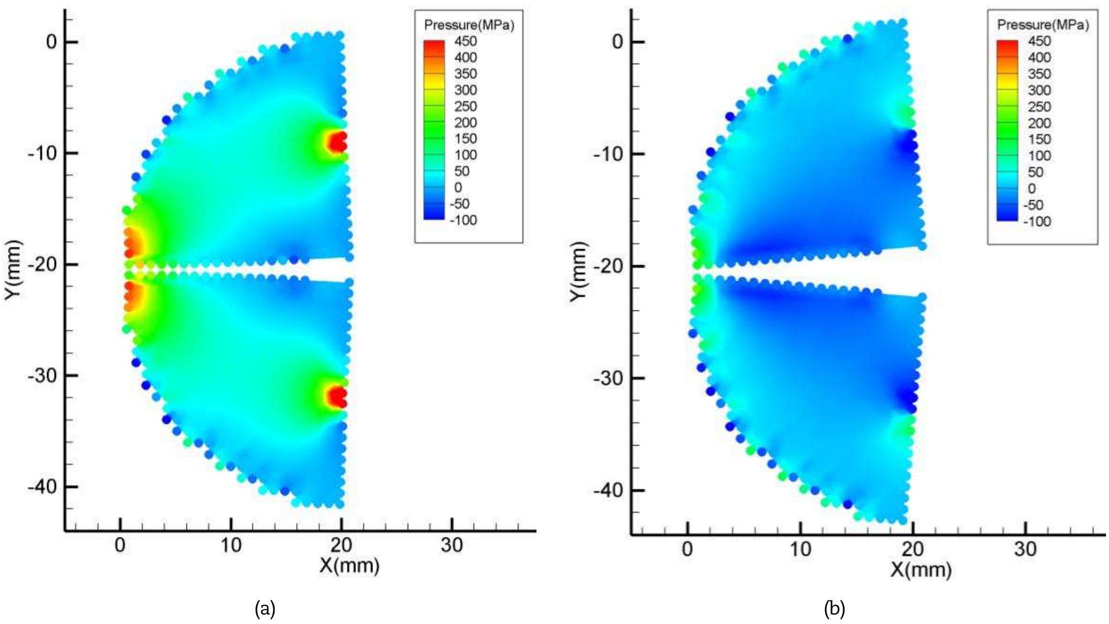

Fig. 11. Pressure distribution in the SCB specimen of granite at different times, (a) t = 55 μs, (b) t = 110 μs.

Figure 12(a) presents a high-speed camera image of the SCB specimen's fracture and fragmentation at t = 160 μs, while Fig. 12(b) shows the numerical simulation result at the same time. It can be observed that at t = 160 μs, the rotation angle of the fragment was 10.2° from the calculation and 9.0° captured by the high-speed camera. The numerical and experimental results are in reasonable agreement, indicating that the numerical model can well reflect the crack propagation behavior of the SCB specimen.

The simulated crack propagation velocity and fragment rotation angle are quantitatively compared with experimental data and conventional FDEM results in Table 6. The maximum relative error of crack velocity predicted by the proposed method is 13.06%, and the fragment deflection error is 13.33%, which is significantly lower than that of conventional FDEM (19.03% and 27.78%). The simulated fracture morphology and dynamic fragmentation behavior are in good agreement with high-speed camera observations, verifying the superior fracture characterization accuracy of the adaptive coupling method.

4.4. Penetration of concrete slabs

A projectile penetration test on a concrete slab is simulated to validate the performance of the proposed method in solving large-deformation penetration and spalling problems. The projectile was made of steel, with a diameter of 2 cm and a total length of 2.5 cm. The concrete slab had a thickness of 3 cm and a length of 8 cm. The projectile was launched toward the concrete slab at an initial velocity of 200 m/s. A bilinear elastic-plastic constitutive model was adopted for the steel projectile, while the concrete was modeled using an ideal elastic-plastic constitutive model combined with the Mohr-Coulomb fracture model incorporating a tension cut-off criterion. The material parameters used in the calculation are presented in Table 5.

Both the steel projectile and the concrete slab were initially set as FEs, and the adaptive FE–DEM conversion is automatically activated in impact cratering and spalling regions, effectively avoiding severe mesh distortion and failure encountered in pure FEM simulation (as shown in Fig. 13). The steel projectile was divided into 548 FEs, and the concrete slab was initially divided into 1728 FEs, with an element side length of 1.667 mm. The time increment in the calculation was set to 1.667×10^{-10} s.

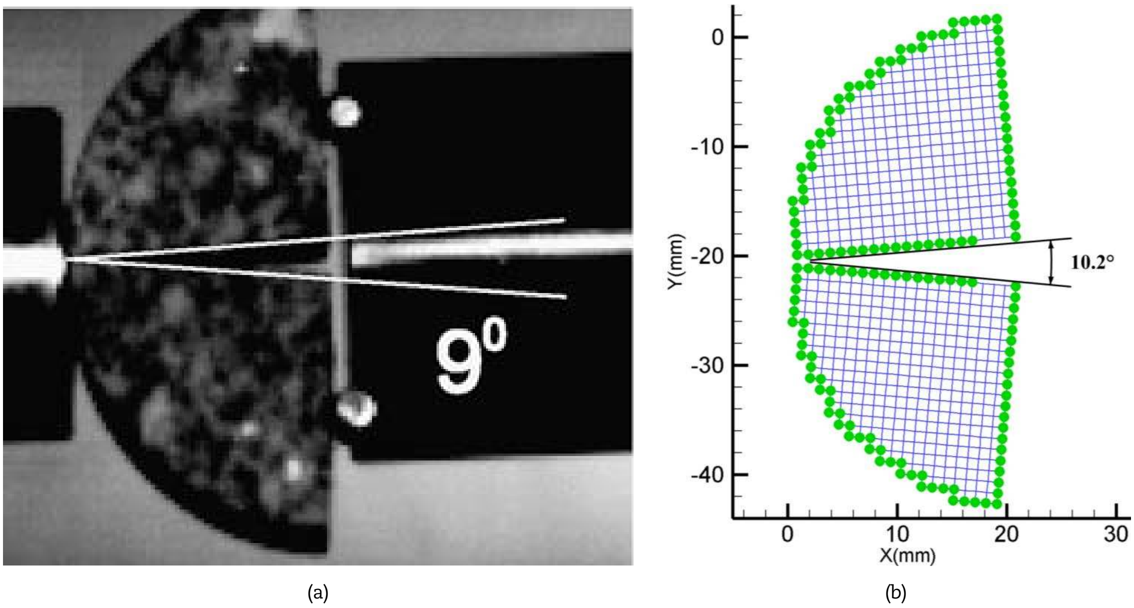

Fig. 12. Fracture and fragmentation of the SCB specimen at t = 160 μs, (a) High-speed camera image, (b) Numerical result.

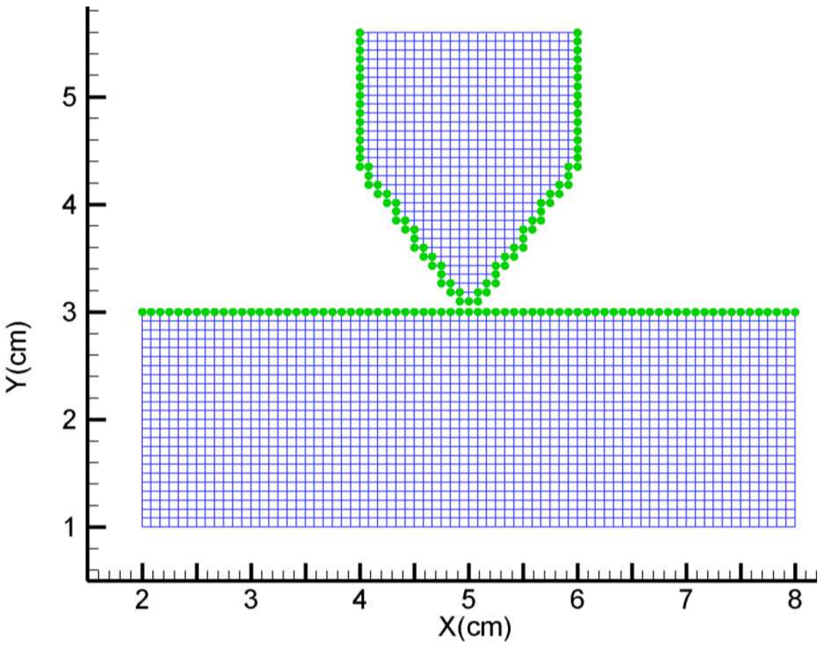

Fig. 13. Modeling of the concrete slab penetration.

Table 6. Quantitative comparison of fracture characteristics.

Parameter	Experiment	Proposed method	Relative error	Conventional FDEM	Relative error
Crack velocity 1 (m/s)	268	233	13.06%	217	19.03%
Crack velocity 2 (m/s)	355	361	1.69%	339	4.51%
Fragment rotation angle (°)	9.0	10.2	13.33%	11.5	27.78%

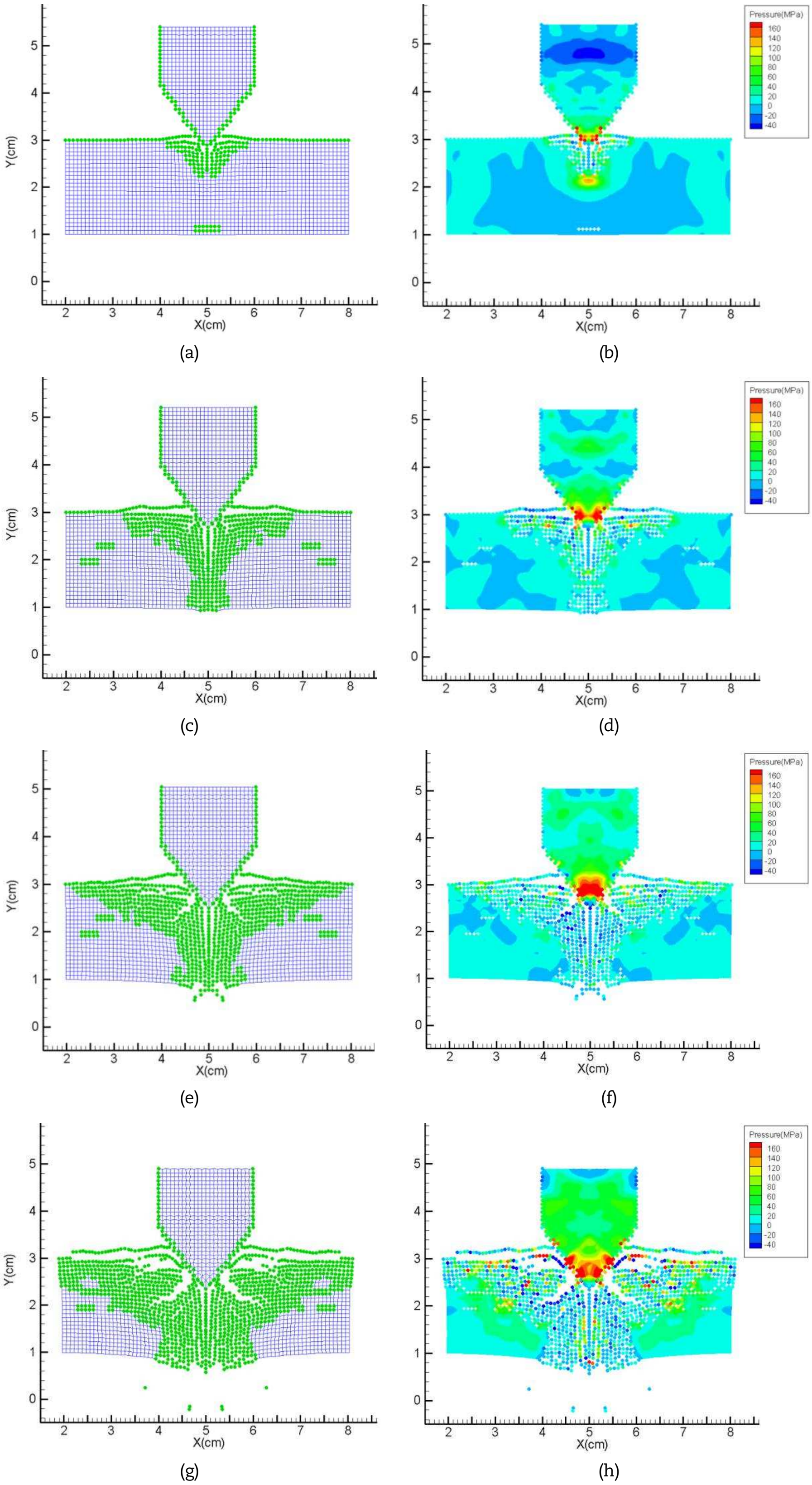

Fig. 14. Numerical results of projectile penetration at different time instants, Penetration at, (a) t = 20 μs, (b) t = 20 μs, (c) t = 40 μs, (d) t = 40 μs, (e) t = 60 μs, (f) t = 60 μs, (g) t = 80 μs, (h) t = 80 μs.

The numerical results at different time instants are shown in Fig. 14. As can be seen from the figures, the numerical results successfully capture the whole process of concrete cratering, surface spalling and internal crack propagation, which is consistent with the typical dynamic failure characteristics of concrete under impact penetration. This case further verifies that the proposed adaptive coupling method can stably solve complex large-deformation discontinuous failure problems that cannot be handled by traditional continuum methods.

4.5. Comparative analysis with alternative numerical methods

To highlight the performance advantages of the proposed adaptive FEM–DEM coupling method, this section systematically compares it with three mainstream numerical approaches, namely pure FEM, pure DEM, and conventional FDEM, based on the foregoing numerical cases.

In the stress wave propagation case in Section 4.1, pure FEM performs well in continuous wave simulation but fails to model post-failure discontinuities due to mesh distortion and mass loss. Pure DEM can capture discrete behaviors but yields slight deviations in stress and wave responses. Conventional FDEM and fixed FEM–DEM coupling relies on predefined interfaces and cannot ensure continuous wave transmission. In contrast, the proposed method realizes stable wave propagation across adaptive FEM–DEM boundaries, with particle velocity and shock wave velocity errors controlled within 4% and 3%, respectively, demonstrating reliable interfacial consistency.

The efficiency analysis in Section 4.2 verifies the method's superior accuracy-efficiency balance. Pure DEM suffers from sharply increased computational cost with growing particle numbers, while pure FEM is efficient but incapable of simulating fracture. Unlike fixed coupling schemes, the proposed method adaptively arranges DEM only in damage-prone regions and retains efficient FEM discretization in intact domains. Its computational cost is merely 45%–47% of full-domain DEM, greatly improving simulation efficiency.

For the SCB dynamic fracture test in Section 4.3, pure FEM cannot spontaneously reproduce impact-induced crack propagation and relies on artificial fracture parameters. Pure DEM requires ultra-fine discretization and entails high computational consumption. Conventional FDEM lacks adaptive domain adjustment, leading to inaccurate crack velocity and fragment motion. The proposed damage-triggered adaptive coupling method accurately captures dynamic fracture characteristics, with the minimum crack velocity error reaching 1.69%, and the simulated fracture morphology matches well with experimental observations.

In the concrete penetration case in Section 4.4, pure FEM fails owing to severe mesh distortion under large deformation and fragmentation. Pure DEM can simulate discrete failure but cannot reflect global structural deformation. Conventional FDEM adopts static fracture processing and fails to update continuum/discontinuum domains with material damage, producing unreasonable penetration morphology. The proposed method achieves automatic FEM-to-DEM conversion in severely damaged areas, effectively avoiding mesh failure and reliably reproducing cratering, spalling and fragmentation behaviors. In summary, compared with conventional numerical methods, the proposed adaptive FEM–DEM algorithm presents better interfacial stability, higher computational efficiency and stronger adaptability to complex impact dynamic and progressive fracture problems.

The superior performance of the proposed adaptive FE–DEM coupling method stems from its damage-driven dynamic domain adjustment strategy. Traditional fixed coupling, XFEM and standalone numerical methods are constrained by mesh distortion, redundant discretization and poor fracture adaptability. In contrast, the present method retains efficient FEM computation for intact continuum regions and adaptively converts severely damaged finite elements into discrete particles to capture post-failure deformation and fragmentation. This mechanism combines the strengths of continuum and discontinuum algorithms, achieving an optimal balance of accuracy and efficiency for impact fracture simulations. However, this method has clear limitations and applicability boundaries. The plastic strain-based conversion criterion works reliably for progressive fracture under medium-to-high strain-rate loading but may induce minor numerical perturbations under ultra-high strain-rate explosive failure. Furthermore, the current 2D planar framework and simplified bilinear elastoplastic constitutive model cannot fully reproduce three-dimensional structural failure and refined post-peak softening of quasi-brittle materials. The adopted fracture criterion is relatively single, and the method exhibits slight mesh dependency under fine discretization. In addition, existing validations are restricted to laboratory-scale tests, lacking large-scale industrial benchmark verification. To overcome these deficiencies, future work will extend the method to a full 3D framework, adopt advanced constitutive models for complex nonlinear material responses, develop multi-material interface processing and thermal effect coupling modules, and optimize parallel computing implementation to improve efficiency and enable large-scale engineering impact simulations.

5. Conclusions

This study develops an adaptive FE-DEM coupling algorithm and corresponding computational program for impact dynamic simulations, fully synergizing the strengths of FEM in continuous deformation calculation and meshless DEM in characterizing discontinuous fracture and fragmentation. The core methodological contribution lies in the plastic damage-driven automatic FE-to-DEM conversion strategy, which eliminates artificial coupling region definition and mesh remeshing dependence. Strict conservation of mass, momentum, and energy is guaranteed during domain transformation, and matched interface discretization together with unified time-step criteria and optimized element-particle size matching effectively suppresses numerical oscillation and field mutation, significantly improving the numerical robustness and reproducibility of the coupling system. Comparative case studies on plate wave propagation, granite dynamic fracture, and concrete slab penetration validate the reliability and feasibility of the proposed algorithm. Compared with conventional numerical methods, the developed approach exhibits prominent computational advantages in solving large-deformation progressive failure problems, balancing high simulation accuracy and stable computational efficiency. This method provides a reliable technical solution for impact-induced continuous deformation, crack propagation and material fragmentation, possessing important practical engineering significance for dynamic fracture analysis and anti-impact structural design of geotechnical and building materials. Despite the above merits, this work still has certain limitations, including the adopted simplified DEM constitutive model and restricted applicability to complex multi-material and extreme impact failure scenarios. Future research will focus on optimizing and enriching material constitutive models to extend the algorithm's applicability to diverse specialized materials and complex dynamic failure behaviors, further promoting the engineering application of the continuum–discontinuum coupling method in impact dynamics.

Author Contributions

Z. Li planned the scheme and suggested the validations; X. Cheng conducted the research, initiated the project, and analyzed the results; B. Jiang developed the mathematical modeling and examined the theory validation. The manuscript was written through contributions of all authors. All authors discussed the results, reviewed, and approved the final version of the manuscript.

Acknowledgments

This work is supported by the National Natural Science Foundation of China (Project No. 12372344), which is gratefully acknowledged.

Conflict of Interest

The authors declared no potential conflicts of interest concerning the research, authorship, and publication of this article.

Funding

The authors received no financial support for the research, authorship, and publication of this article.

Data Availability Statements

The datasets generated and/or analyzed during the current study are available from the corresponding author on reasonable request.

References

[1] Pian, T.H.H., Tong, P., Finite element methods in continuum mechanics, *Advances in Applied Mechanics*, 12, 1972, 1-58.
[2] Voisin-Leprince, M., Garcia-Suarez, J., Anciaux, G., Molinari, J.-F., Two-scale concurrent simulations for crack propagation using FEM–DEM bridging coupling, *Computational Particle Mechanics*, 11, 2024, 2235-2243.
[3] Xu, Q., Ye, J., An adaptively coupled DEM–FEM algorithm for geometrical large deformation analysis of member structures, *Computational Particle Mechanics*, 7, 2020, 947-959.
[4] Cornejo, A., Mataix, V., Zárate, F., Oñate, E., Combination of an adaptive remeshing technique with a coupled FEM–DEM approach for analysis of crack propagation problems, *Computational Particle Mechanics*, 7, 2020, 735-752.
[5] Cundall, P.A., Strack, O.D.L., A discrete numerical model for granular assemblies, Géotechnique, 29, 1979, 47-65.
[6] Volcy, S.H.E., Sibille, L., Chareyre, B., Dano, C., Hosseini-Sadrabadi, H., An adaptative discretization to model boundary value problems with discrete element method, *Granular Matter*, 27, 2025, 41.
[7] Vyas, D.R., Ottino, J.M., Lueptow, R.M., Umbanhowar, P.B., Improved velocity-Verlet algorithm for the discrete element method, *Computer Physics Communications*, 310, 2025, 109524.
[8] Lu, J., Cao, G., Li, C., Hu, S., Implicit bonded discrete element method with manifold optimization, *ACM Transactions on Graphics*, 44, 2025, 1-17.
[9] Zhang, K., Yan, H., Lu, J.-M., Ren, B., Rod-bonded discrete element method, *Graphical Models*, 133, 2024, 101218.
[10] Yang, Q., Wang, Z., Yang, T., Chen, B., Li, L., Lin, Z., A resolved and unresolved discrete element method coupled with volume of fluid method, *Powder Technology*, 458, 2025, 120993.
[11] Landgraeber, J., Bruening, F., Discrete element method in polymer processing – Method for development of material models, *Advanced Powder Technology*, 36, 2025, 104968.
[12] Boucher-Bergstedt, C., Jankauski, M., Johnson, E., Buzz pollination: investigations of pollen expulsion using the discrete element method, *Journal of the Royal Society Interface*, 22, 2025, 20240526.
[13] Liang, Z., Zhou, Z., Huang, Y., Yang, H., Assessing apple bruise susceptibility using the discrete element method, *Journal of Food Engineering*, 394, 2025, 112517.
[14] Kyalo, M.N., Kimotho, J.K., Ndiritu, H.M., Performance evaluation of polygonal and cylindrical ball mills using discrete element method, *Engineering Reports*, 7, 2025, e13043.
[15] Munjiza, A., Bangash, T., John, N.W.M., The combined finite–discrete element method for structural failure and collapse, *Engineering Fracture Mechanics*, 71, 2004, 469-483.
[16] Bouckaert, I., Godio, M., Pacheco de Almeida, J., Hybrid discrete-finite element method for biaxially-discretized structures, *Structures*, 71, 2025, 107954.
[17] Kumbhar, P., Swaminathan, N., Annabattula, R.K., Mesoscale analysis of Li-ion battery microstructure using sequential coupling of discrete element and finite element method, *International Journal of Energy Research*, 46, 2022, 12003-12025.
[18] Færgestad, R.M., Holmen, J.K., Berstad, T., Cardone, T., Ford, K.A., Børvik, T., Coupled finite element-discrete element method (FEM/DEM) for modelling hypervelocity impacts, *Acta Astronautica*, 203, 2023, 296-307.
[19] Deng, P., Liu, Q., Failure mechanism of a tunnel in a soil–rock mixture based on a new combined finite–discrete element method, *European Journal of Environmental and Civil Engineering*, 29, 2025, 438-470.
[20] Hubert, C., Attaoui, Y.E., Leconte, N., Massa, F., A coupled finite element-discrete element method for the modelling of brake squeal instabilities, *European Journal of Mechanics - A/Solids*, 108, 2024, 105427.
[21] Cao, R., Li, Y., Feng, C., Fan, L., Liu, W., Zhang, Y., Study on the damage effects of explosive media based on FEM-DEM local adaptive transformation, *Geotechnical and Geological Engineering*, 42, 2024, 339-350.
[22] Liu, K., Liu, W., Application of discrete element method for continuum dynamic problems, *Archive of Applied Mechanics*, 76, 2006, 229-243.
[23] Liu, K., Gao, L., Tanimura, S., Application of discrete element method in impact problems, *JSME International Journal Series A Solid Mechanics and Material Engineering*, 47, 2004, 138-145.
[24] Schinner, A., Fast algorithms for the simulation of polygonal particles, *Granular Matter*, 2, 1999, 35-43.
[25] Labuz, J.F., Zang, A., Mohr–Coulomb failure criterion, *Rock Mechanics and Rock Engineering*, 45, 2012, 975-979.
[26] Chen, R., Xia, K., Dai, F., Lu, F., Luo, S.N., Determination of dynamic fracture parameters using a semi-circular bend technique in split Hopkinson pressure bar testing, *Engineering Fracture Mechanics*, 76, 2009, 1268-1276.

ORCID iD

Zhibin Li https://orcid.org/0000-0003-4531-2115

© 2026 Shahid Chamran University of Ahvaz, Ahvaz, Iran. This article is an open access article distributed under the terms and conditions of the Creative Commons Attribution-NonCommercial 4.0 International (CC BY-NC 4.0 license) (http://creativecommons.org/licenses/by-nc/4.0/).

How to cite this article: Li Z., et al., A 2D Adaptive Finite Element-Discrete Element Coupling Algorithm for Impact Dynamics, *J. Appl. Comput. Mech.*, xx(x), 2026, 1–15. https://doi.org/ 10.22055/jacm.2026.49257.5844

Publisher's Note Shahid Chamran University of Ahvaz remains neutral with regard to jurisdictional claims in published maps and institutional affiliations.